1.2   MID-ATLANTIC FRONTAL WAVE DEVELOPMENT, BOUNDARY LAYER STRUCTURE, AND SURFACE FLUXES IN FASTEX IOP1: OBSERVATIONS AND SENSITIVITY EXPERIMENTS

P. Ola G. Persson, L. B. Nance, J. Hare and A. White
CIRES/NOAA/ETL, Boulder, CO 80305

1. INTRODUCTION

The Fronts and Atlantic Storm Tracks Experiment (FASTEX) was conducted in the North Atlantic Ocean during January-February 1997. The overall objective of FASTEX was to advance the scientific understanding necessary to enable detailed diagnosis and prediction of the life cycles of eastern oceanic storms and their associated cloud and precipitation systems (Joly et al. 1999). During December 22, 1996, - January 26, 1997, this project had a joint NOAA and NSF funded air-sea interaction component that used the Woods Hole *R/V Knorr* as a platform for various flux and remote sensing measurements. The primary objectives of this component were to:

1) collect surface flux measurements in a high wind speed, open-ocean environment, the associated sea-state measurements, and quasi-continuous measurements of the mid-oceanic atmospheric boundary layer structure;

2) validate and improve parameterization schemes of the high-wind marine environment;

3) demonstrate the impact of improved parameterizations and/or mid-oceanic boundary-layer measurements on marine extratropical cyclone development and forecasting; and

4) validate satellite and aircraft estimates of surface and near-surface characteristics.

The inclusion of the air-sea interaction measurements within a large field program assures downwind validation data with mesoscale detail for assessment of the impact of PBL fluxes, and the data necessary for the understanding the spatial relationships between surface fluxes and frontal features.

This paper focuses on objective 3, the validation and improvement of surface flux and atmospheric boundary layer parameterizations in a high-wind, maritime environment. This work describes observations and simulations of FASTEX Intensive Observing Period 1 (IOP1) on Jan. 9-10. A succession of three weak frontal waves developed on the southern side of a large cyclone covering the North Atlantic Ocean. Some of these waves developed into deep cyclones while others remained weak waves.

The observations and validation data were primarily made on board four ships located in the central North Atlantic, which were dedicated to the FASTEX field program. We will emphasize the boundary-layer structure and surface fluxes at the *R/V Knorr*. The

Corresponding author address: Dr. Ola Persson, CIRES/NOAA/ETL, R/ET7, 325 Broadway, Boulder, CO 80305; e-mail: opersson@cires.colorado.edu

modeling work utilizes the Penn State/NCAR MM5 model to test the sensitivity of the frontal wave development and the mid-oceanic boundary layer structure to the boundary layer parameterization scheme.

2. OBSERVATIONAL SYSTEM

The *R/V Knorr* contained a large suite of instrumentation focused on measuring surface fluxes of momentum, sensible heat and latent heat using the covariance, inertial dissipation, and bulk methods; wave-height spectra necessary for interpretation of the surface fluxes; and the boundary layer kinematic and thermodynamic structure. Instruments included standard meteorological instruments, flux instruments (e.g., sonic anemometer, Ophir hygrometer) mounted on a pivoting bow mast designed to allow maintenance and periodic cleaning from an upper deck; a TSK wave-height recorder supplied by the Bedford Institute of Oceanography; a NCAR 915-MHz wind profiler on a gyro-stabilized platform providing winds and wind spectra every 30 min between 1-6 km; a vertically pointing aerosol/cloudbase lidar providing cloud base and PBL height; OMEGA soundings at least every 6 hours (every 1.5-3 hours during IOPs); broadband Eppley radiometers providing fluxes of downwelling longwave and shortwave radiation; a vertically pointing, Doppler S-band radar with enhanced sensitivity providing cloud and precipitation structure; a NCAR optical raingauge and a University of Kiel ship raingauge; and videotapes of the sea-state. Table 1 provides a list of some of these instruments and their salient characteristics. More complete descriptions of the instrumentation and the data processing are provided by Persson et al. (1997, 2003a,b), and Hare et al. (1999).

Analyses from the French ARPEGE forecasting system and the European Center for Medium-Range Weather Forecasting (ECMWF) were used to provide spatial analyses. Validations of these analyses using the array of surface buoys and ships available in the North Atlantic for FASTEX have revealed no significant discrepancies for IOP1 (e.g., see Fig. 10).

3. IOP1 OBSERVATIONS

3.1 *Synoptic Evolution*

During IOP1, one decaying cyclone and three frontal waves were present in the North Atlantic Ocean. These are designated as W0 and W1-W3, respectively, in Fig. 1. Each of the three waves W1-W3 tracked either right along or just to the southeast of the strong SST gradient between the warm mid-Atlantic Gulfstream

Table 1: Instrumentation on board the R/V Knorr

| Instrument	Parameter(s)	Spatial (height) coverage	Temporal resolution
Standard Met Parameters	p, T, RH, WS, WD	19 m	1 min
Sonic Anemometer	τ, H_s	19 m	10 Hz
Ophir Hygrometer	H_l	18 m	20 Hz
"Sea Snake"	T_s	N/A	1 min
Optical rain gauge	Rain Rate	N/A	1 min
Eppley Broadband Radiometers	LW_d, SW_d	N/A	1 min
CLASS Soundings	p, T, RH, WS, WD	0-18 km	1.5-6 h
915 MHz Wind Profiler	WS, WD, C_n^2	1-6 km	30 min
S-band Vertically Pointing Radar	precip and cloud reflectivity	0-10 km	30 s
Ceilometer	cloud base	0-12 km	15 s
TSK Wave Height recorder	wave height spectra	N/A	2 Hz
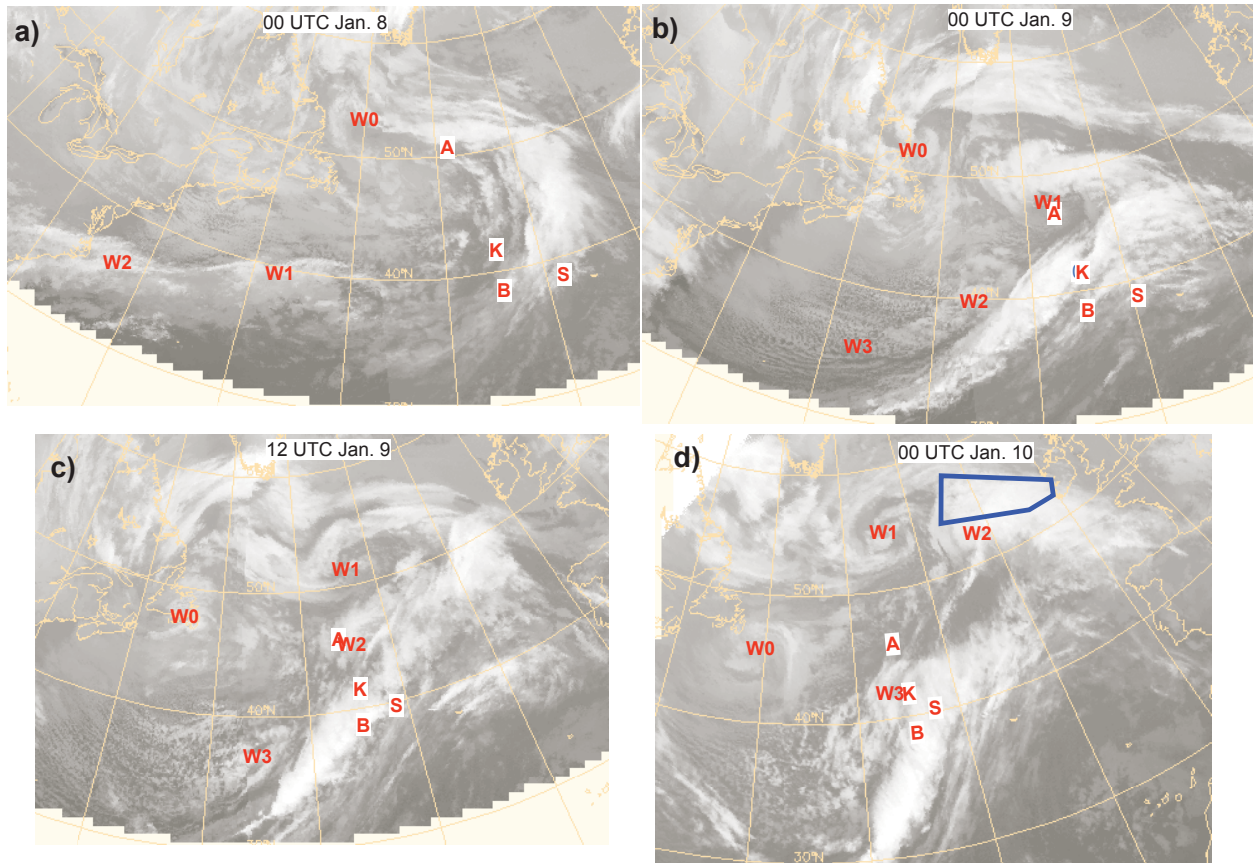
Fig. 1: Satellite IR mosaics for a) 00 Z Jan. 8, b) 00 Z Jan. 9, c) 12Z Jan. 9, and d) 00Z Jan. 10. The positions of the 4 frontal waves, W0-W3 are shown. The locations of the upstream research ships Knorr, *(K),* Suroit *(S),* Victor Bugaev *(B), and* Aegir *(A) are shown in each pane. The main frontal wave sampled in the ship area on Jan. 9 is labeled W, while the downstream mesoscale sampling area (MSA) where wave W2 was sampled by three aircraft is shown enclosed in blue in d).*
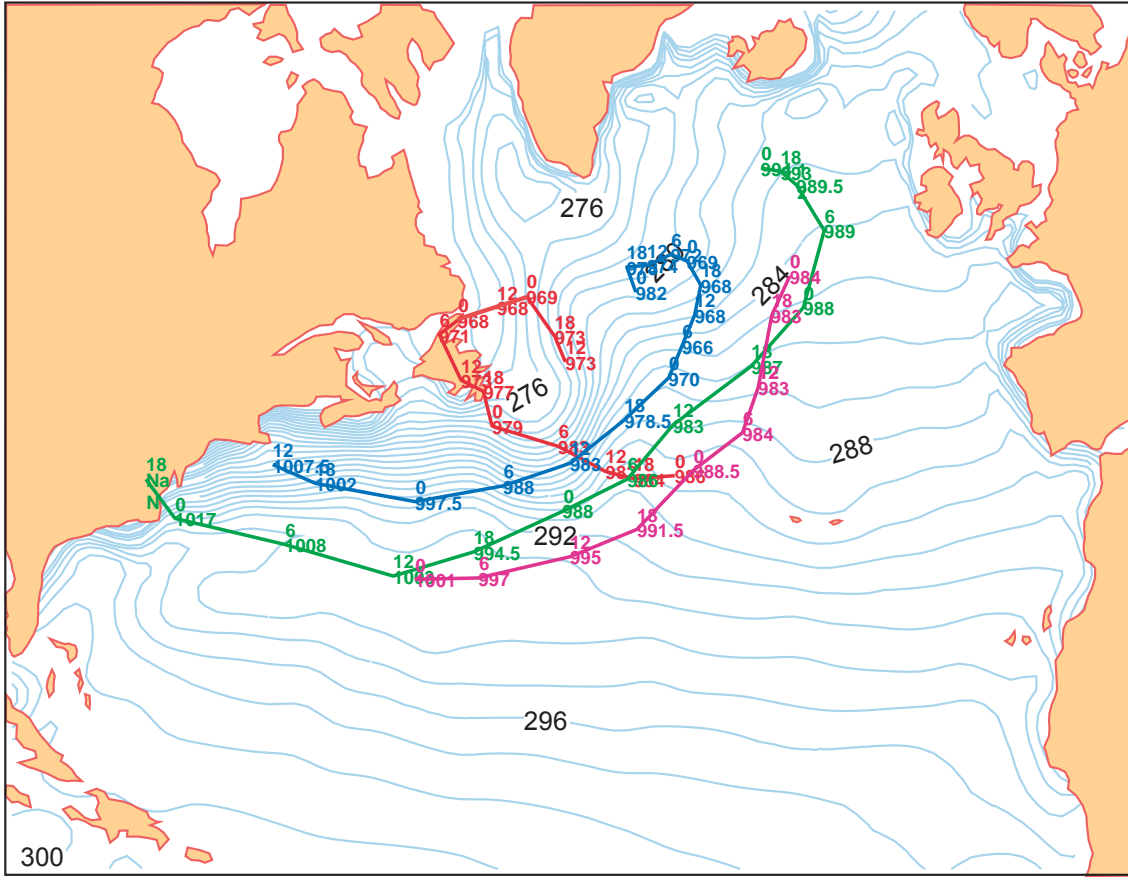
Fig. 2: Tracks of the low-pressure center for waves W0 (red), W1(blue), W2 (green), and W3 (purple) as given by the ECMWF analyses and IR satellite images between 12 UTC Jan. 7 and 00 UTC Jan. 11. Each 6 hourly location is marked with the hour and central pressure (hPa). Also shown is the surface temperature (K) analysis at 12 UTC Jan. 7 used in the MM5 simulations.

and the cold Labrador current (Fig.2). The decaying cyclone W0 moved northwestward over the cold waters and later southeastward back over the Gulfstream waters. Each of the three frontal waves showed some development, with wave W1 developing into the strongest storm (Fig. 3).
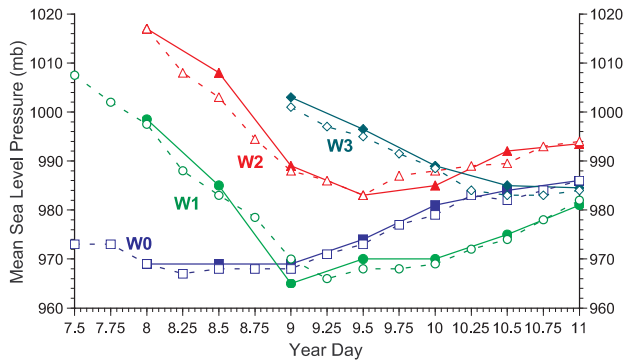

Fig. 3: Central pressure for the four waves as depicted in the ECMWF (solid symbol) and ARPEGE analyses (open symbol).

All three of the frontal waves were sampled by the mid-Atlantic ship array (Fig.1). Wave 2 was also sampled by the research aircraft near the coast of Ireland in the mesoscale sampling area (MSA). At the *R/V Knorr*, the surface data (Fig. 4) clearly show the pressure troughs associated with each wave, and transitions in air temperature, humidity, wind speed and wind direction typically associated with mid-latitude frontal passages. The prefrontal, warm-sector, low-level jets (LLJs) associated with W1 and W2 produced winds near 17-19 m s^{-1} at the 19 m height for 3-5 hours at the ship. For W3, the low center passed directly over the ship so the *Knorr* was not in the warm-sector and no LLJ is discernible. Frontal passages produced air temperature changes of about 3-5°C and specific humidity changes of about 2-3 g kg^{-1}.

3.2 Boundary-layer Structure

Time-height sections from the sounding data show the vertical structure in the lowest 2500 m associated with the passage of the waves at the *Knorr* (Fig. 5). A prominent warming and moistening occurred in the 6-8 hours prior to the frontal passages associated with the
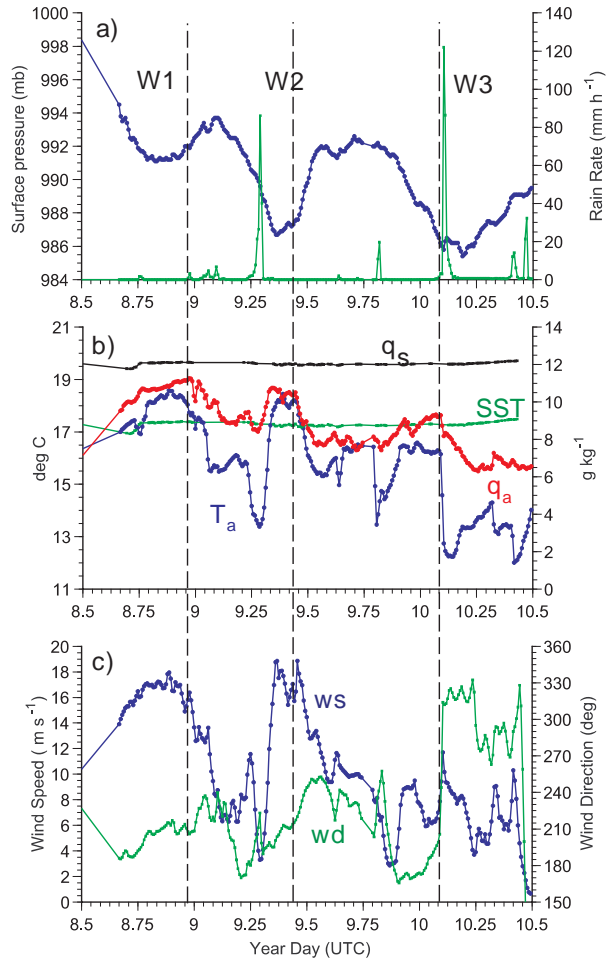
3

Fig. 4: Time series from the R/V Knorr of a) surface pressure (blue) and precipitation rate (green), b) air temperature (T_a), sea-surface temperature (SST), air specific humidity (q_a), and surface specific humidity (q_s), and c) wind speed (ws) and wind direction (wd). The pressure trough associated with frontal waves W1-W3 are shown in a), and the passage of the front associated with each trough at the surface are indicated by the vertical dashed lines.

first two waves. Warming occurs up to at least 2500 m, while most of the moistening occurs below 1200 m. A prominent LLJ of 34 m s^{-1} centered at 1500 m occurs with W1. There is no obvious low-level wind maximum associated with the strong winds just prior to frontal passage in W2 from the soundings, but the wind profiler with its better temporal resolution shows a prefrontal maximum of 36 m s^{-1} near 1650 m and another of the same strength near 2200 m (not shown). The duration of this LLJ is only about 2.5 hours. With wave W3, the slight warming occurs principally between 700-2000 m, and the slight moistening occurs principally at the surface. The former suggests the passage of an occluded portion of the frontal system. The virtual potential temperature (θ_v) and equivalent potential temperature (θ_e) cross-sections show that the prefrontal air is statically stable ($\partial\theta_v / \partial z > 0$) but generally

potentially unstable ($\partial\theta_e / \partial z < 0$). The post-frontal boundary layer air tends to be statically neutral.

The height of the boundary layer is not always easy to estimate. The θ_v cross-section shows periods of enhanced stability likely associated with the top of the boundary layer, especially in the post-frontal regions. In the prefrontal air, where no obvious stable layer exists, the strong vertical moisture gradient can be taken as the top of the boundary layer. The cloud base height as determined from the ceilometer agrees well with these estimates. The cloud bases also agree well with the top of enhanced reflectivity from the S-band radar (Fig. 6). Therefore, we use these cloud base estimates as proxies for the boundary layer height. Hence, we see that the prefrontal PBL height is about 700-1200 m, while the post-frontal PBL height varies from 800-2000 m. Note that the LLJ associated with wave W1 is located just above the PBL in Fig. 5d.

The S-band radar (Fig. 6) shows that the clouds are quite deep (up to 8 km) with the trailing front from wave W1, while only a brief shower with cloud depth of 5 km occurs with the frontal passage associated with wave W2. The satellite sequence (Fig. 1c-d) suggests that the deep cloud shield of wave W2 sampled in the MSA was primarily warm frontal and developed subsequent to passing over the *Knorr*. The clouds associated with wave W3 also extend to a height of about 8 km at the *Knorr*.

3.3 *Surface Fluxes at the R/V Knorr*

The surface stress (τ) and fluxes of sensible heat (H_s) and latent heat (H_l) are strongly modulated by the synoptic changes (Persson et al 2003a, b). Surface stresses reached 1.0-1.2 N m^{-2} under the LLJ in the prefrontal air (Fig. 7). H_s tended to be slightly negative ($\sim$ -30 W m^{-2}) as the warm-air advection just before frontal passage produced air warmer than the local SST (see Fig. 4). However, although the specific humidity did increase in the prefrontal air, it never reached the saturated specific humidity given by the SST. Hence, H_l was positive and between 50-150 W m^{-2} in the prefrontal air. Though the wind speed decreased in the post-frontal region, H_s and H_l increased significantly to 25-50 W m^{-2} and 100-180 W m^{-2}, respectively, because the air temperature and specific humidity decreased.

4. MODELING TESTS

4.1 *Model Configuration*

The numerical model used in this study is the nonhydrostatic version of the Pennsylvania State University (PSU) /National Center for Atmospheric Research (NCAR) mesoscale modeling system, otherwise known as MM5 modeling system (Grell et al. 1994). A two-way interactive nested grid configuration was used for this study. The outer domain (D1), which extended from the eastern United States to western Europe and Africa, had a horizontal grid spacing of 81 km (89 by 69 grid points) (see Fig. 8). The inner nest (D2) covered the northern portion of the Atlantic basin
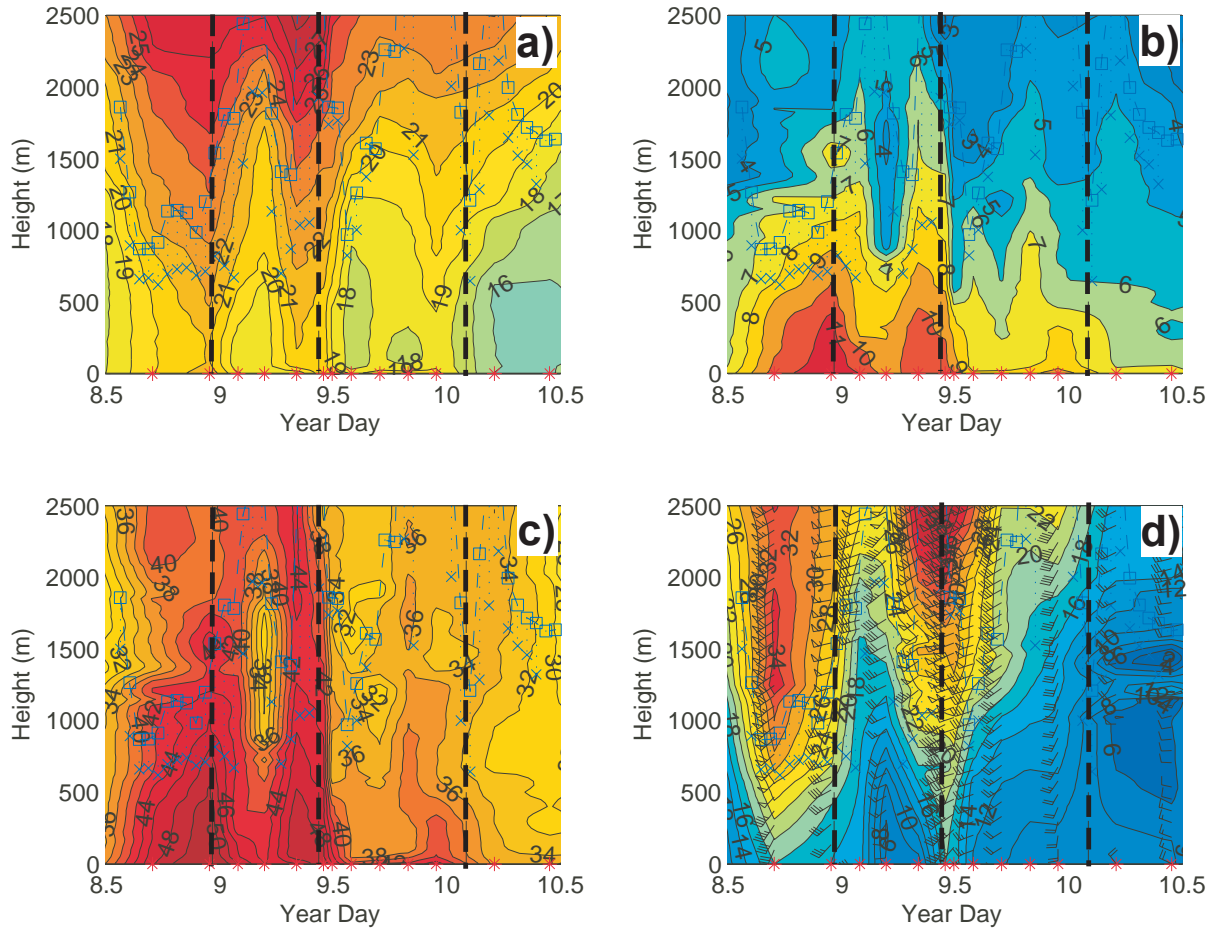
Fig. 5: Time-height sections of a) virtual potential temperature (deg C), b) mixing ratio (g kg^{-1}), c) equivalent potential temperature (deg C), and d) wind speed (m s^{-1}) with wind barbs from soundings on the R/V Knorr. Three-hourly running means of the ceilometer cloud base median (blue square) and the one standard deviation below the median (blue "x") are shown in each panel. The time of each sounding is also marked by a red star along the bottom axis, and the time of each surface frontal passage is shown by the vertical black dashed line.
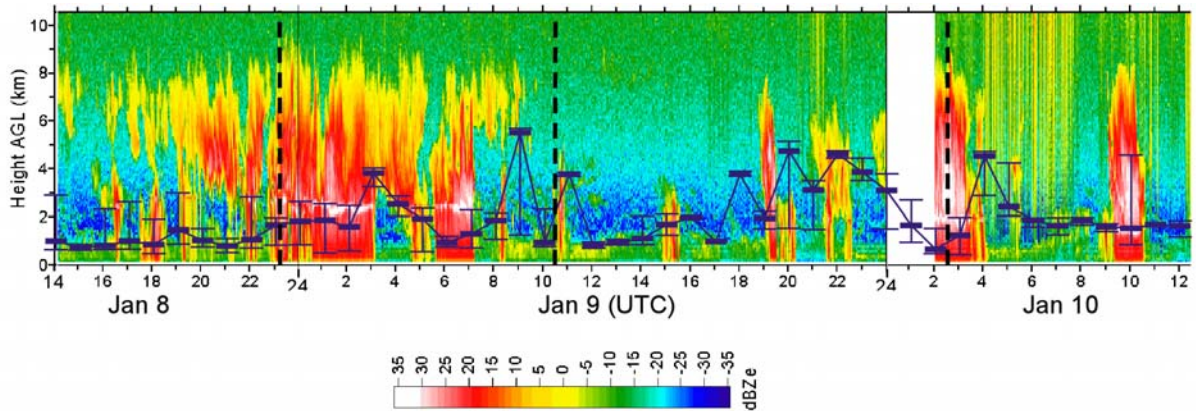

Fig. 6: Time-height section of radar reflectivity from the S-band radar on the R/V Knorr. The hourly ceilometer median cloud base height (heavy dash) is overlaid, with error bars indicating ± one standard deviation around the median. The vertical dashed lines show the time of surface frontal passage.
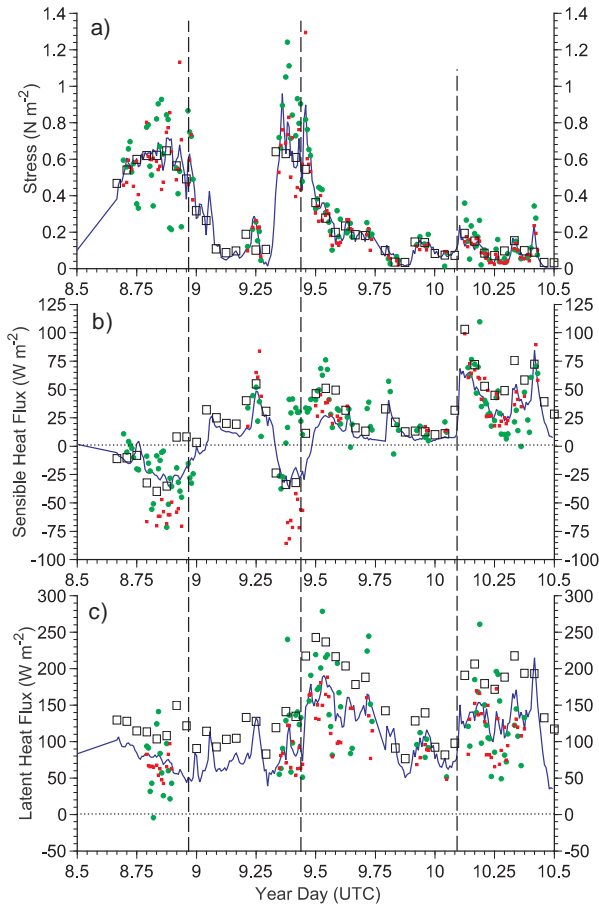
Fig. 7: Ten-minute surface turbulent fluxes from the R/V Knorr. Shown are a) stress, b) sensible heat flux, and c) latent heat flux. The fluxes are calculated from the bulk algorithm of Fairall et al (2003) and the measured bulk parameters (blue line), the inertial dissipation method (red dots), and the covariance technique (green dots). Also shown are the hourly bulk fluxes calculated from the BLK surface flux scheme (Grell et al 1994) discussed in section 4.5.

with a horizontal grid spacing of 27 km (110 by 124 grid points). Fifty unevenly spaced σ layers were used in the vertical between the surface and 10 mb with the maximum resolution in the boundary layer (lowest level at 10 m, 4 levels below 100 m, 20 levels below 1500 m).

Because the impact of surface fluxes on cyclone development can be much delayed (Kuo et al. 1991), a long simulation time was chosen. The model was initialized at 1200 UTC 7 January 1997 and all simulations were carried out for 84 hours (end time 0000 UTC 11 January 1997) with hourly output. Initial atmospheric conditions and sea surface temperatures (SSTs) were generated by first interpolating the European Centre for Medium-Range Weather Forecasts (ECMWF) analyses (2.5° X 2.5°) to the model grid. These analyses were then enhanced with surface and rawinsonde observations, including special FASTEX observations, using a Cressman-type analysis scheme

(Benjamin and Seaman 1985). Additional analyses were generated every 12 h in the same manner and then linearly interpolated in time to provide lateral boundary conditions for the 81-km domain. The SST field (Fig. 2), which was specified using the analysis for
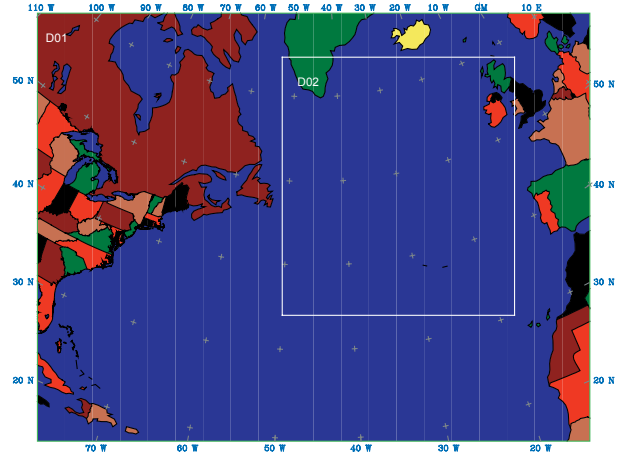

Fig. 8: Domains 1 and 2 for the MM5 simulations.

the initial time, was held constant throughout the simulations.

4.2 Experiments

Four separate simulations were obtained by varying only the planetary boundary layer (PBL) scheme. The PBL schemes considered in this study are: Blackadar (BLK; Blackadar 1976; Zhang and Anthes 1982), Medium-Range Forecasting System (MRF; Hong and Pan 1996), Burk-Thompson (BKT; Burk and Thompson 1989), and Gayno-Seaman (GYS; Shafran et al. 2000). The first two schemes are first-order schemes; the last two are second order schemes and hence include a prognostic equation for the turbulent kinetic energy. The surface flux schemes in the BLK, MRF, and GYS PBL schemes are similar and are based on the Richardson-number dependent parameterization developed by Blackadar (1976) and described by Grell et al. (1994). The surface flux scheme in the BKT PBL scheme is based on the parameterization by Louis (1979).

Each simulation used the Grell cumulus parameterization (Grell 1993), the mixed-phase explicit moisture scheme (Reisner et al. 1998), the cloud-radiation scheme, and the upper-radiative boundary condition (Klemp and Durran 1983). The impact of varying the PBL scheme is presented in terms of a comparison between the observations and output from the simulations generated using a slightly modified version of release 3-5 of the MM5 code.

4.3 Impact on Wave Development and Tracks

At the initial time of the simulations, the dominant features in the ECMWF analysis were a closed low east of Newfoundland Island (cyclone W0) and a weaker
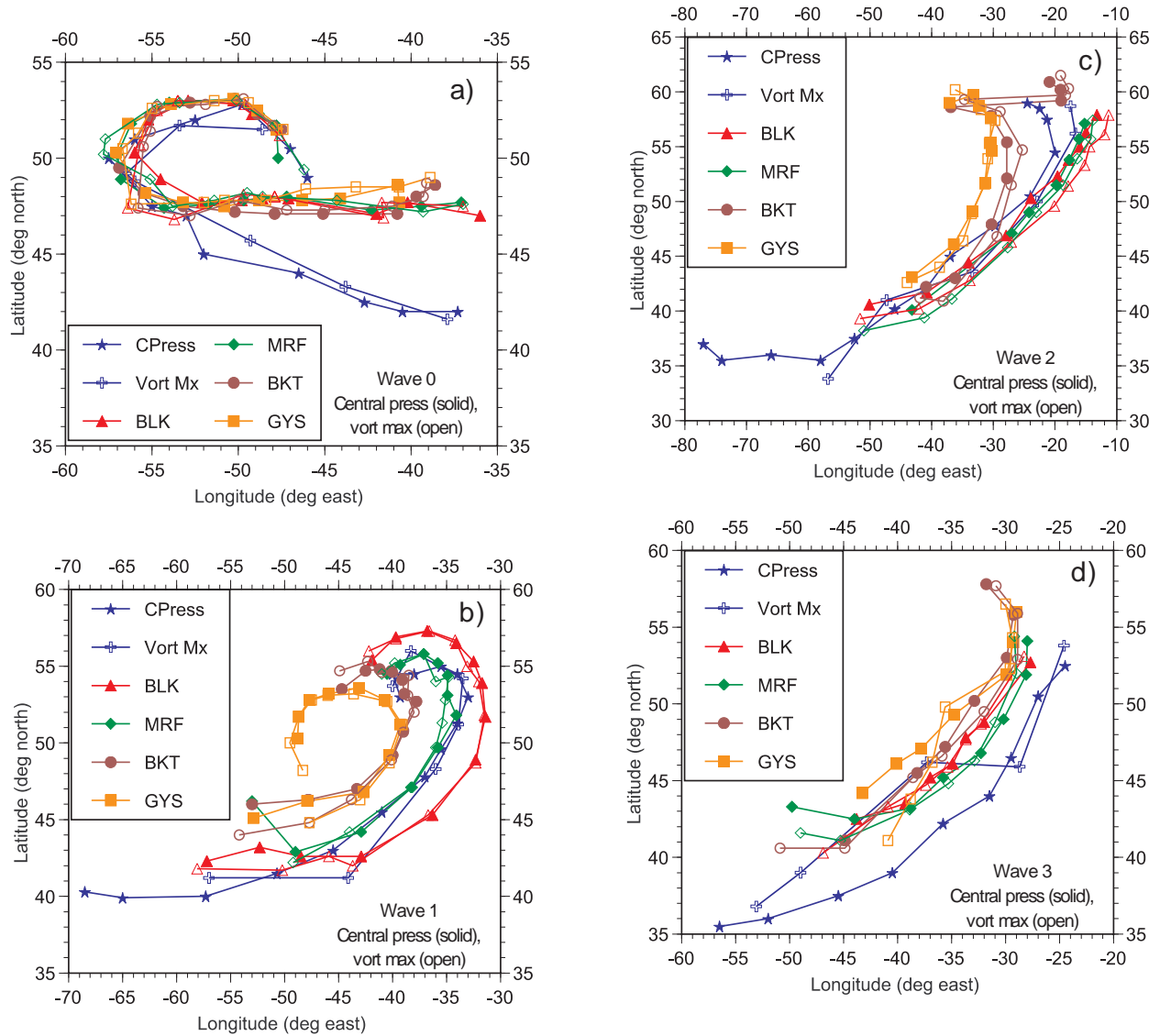
Fig. 9: Tracks of the observed (blue) and modeled waves using different PBL schemes for a) wave 0, b) wave 1, c) wave 2, and d) wave 3. The tracks are defined by the location of the low-pressure center (solid symbol) and the 925 mb vorticity maximum (open symbol). The tracks begin at different times after 12 UTC Jan. 7 depending on when the feature appeared. All tracks end at 00 UTC Jan. 11, except for W1 in GYS, which ends at 18 UTC Jan. 10. Symbols are plotted every 6 hours, except for the observed vorticity maximum, which is plotted every 12 hours.

closed low west of northern Spain (not shown). The objective analysis used to enhance the initial fields for the model simulations moved the low center west of Spain slightly further to the east and introduced a number of shortwave features to the south and southwest of W0.

Between 1200 UTC 7 January and 1200 UTC 9 January, W0 traced a cyclonic path centered on 50° N, 51.5° W and then proceeded in a southeasterly direction over the next 36 h (Figs. 1, 2 and 9a). During the time period the observed W0 moved southeastward, all four simulations propagated this feature along an eastward path. According to the ECMWF and ARPEGE analyses, W0 deepened by 4-6 mb between 1200 UTC 7 January and 0600 UTC 8 January, maintained a fairly constant central pressure for the next 18-24 h as it traced a cyclonic path, and then gradually filled as the wave propagated to the southeast (see Fig. 10a). W0 also underwent an initial deepening phase, followed by a filling phase in each simulation. The BLK and MRF simulations produced a W0 that was slightly weaker during the early part of the simulation, but did a fairly good job representing the dissipation stage of this feature. Conversely, the BKT and GYS simulations produced a W0 with a central pressure that was in better agreement with the analyses during the early portion of the simulation (although the deepening was slightly slower than observed), but maintained a deeper
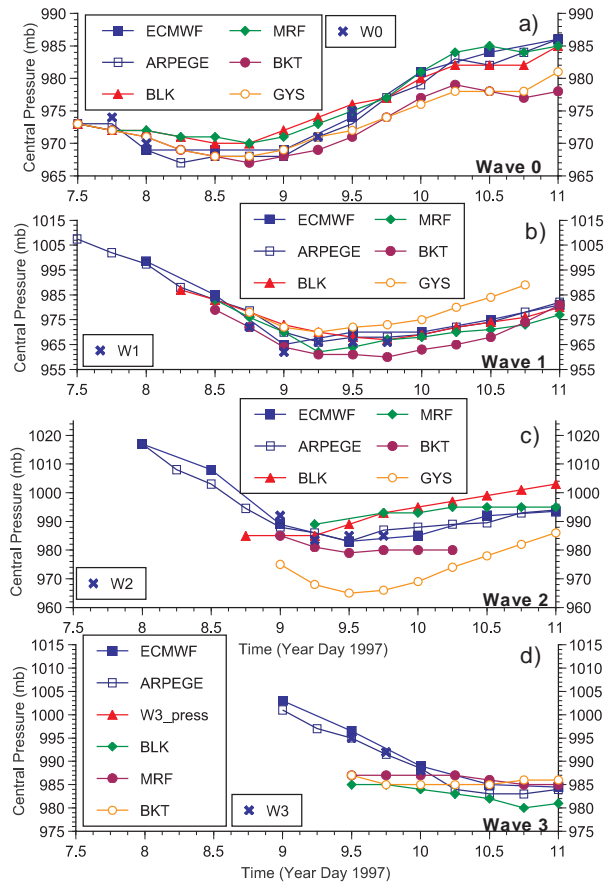
Fig. 10: Evolution of the central pressure in the ECMWF and ARPEGE analyses (blue), manual analyses of surface observations ("x"), and the model runs with the four different PBL schemes for a) wave 0, b) wave 1, c) wave 2 and d) wave 3.

W0 than observed during the latter stage of this wave's life cycle due to a more gradual decay after 0600 UTC 10 January. Although varying the PBL scheme did produce the differences between the numerical simulations noted above, the differences between the simulations were minor in comparison with how they all differed from the observed behavior of W0. Hence, we conclude that varying the PBL scheme did not significantly impact the way the model handled the evolution of W0.

Between 1200 UTC 7 January and 0000 UTC 8 January, wave W1 began to amplify southwest of W0. W1 initially propagated eastward, turned to the northeast, and finally curled back around to the west between 0000 UTC 10 January and 0000 UTC 11 January (Figs. 1, 2 and 9b). The path of the low center in the MRF simulation closely matched that in the analyses, whereas the path in the BLK simulation was to the east of the observed path as the low tracked to the northeast and exhibited a larger radius of curvature as the path curved back to the west. Conversely, the

paths in both the BKT and GYS simulations were to the west of the observed path and exhibited a smaller radius of curvature as the path curved to the west. The observed W1 deepened 42 mb in the 42 hours between 0000 UTC 8 January and 0600 UTC 9 January, followed by a period of gradual filling (Fig. 10b). All four simulations also amplified this wave but to varying degrees. The time period of rapid deepening was well represented in the BKT and MRF simulations, which produced the deepest W1 (central pressures 3-5 mb lower than the lowest observed W1 central pressure). Following the deepening phase, the BKT simulation maintained a stronger W1, while the decay of W1 in the MRF simulation was more on par with the observed behavior. The BLK simulation produced a W1 that was slightly weaker than observed and deepened W1 more gradually over a slightly longer time period. And finally, the GYS simulation produced the weakest W1 (central pressure 4-5 mb higher than observed), but the timing of the deepening and filling phases in this simulation were in good agreement with the observed behavior. Varying the PBL scheme definitely changed the way the model handled W1, with the MRF simulation producing the best overall evolution of this wave.

A second wave, W2, amplified as it propagated around the south and southeast side of W1 and then gradually dissipated as it propagated to the northeast of W1 (Figs. 1, 2, and 9c). This feature was weaker than W1 at all times. It is also the wave that moved closest to Ireland, and was the one sampled by the aircraft in the MSA. W2 in the BLK, MRF, and BKT simulations underwent a similar evolution, whereas W2 in the GYS simulation underwent a rapid intensification, eventually becoming the dominant feature (Fig. 10c). The paths of W2 in the BLK and MRF simulations are very similar (Fig. 9c), being generally to the south and east of the observed path and curving back to the west more gradually than observed. This causes the separation between the observed and simulated paths to increase over the last 12 h of the simulation. Simulations MRF and BLK also have a similar tendency to slightly underestimate the intensification of W2. And yet, the timing of W2 along this path is different in the two simulations, with timing of the MRF W2 being in better agreement with the observed wave (W2 in BLK leads the observed, except during the later portion of the simulation when the timing difference decreases). The path of W2 in the GYS and BKT simulations, once again lies to the west of that observed. Note that the GYS and BKT W2s actually propagated more quickly to the northeast and curved back to the west more rapidly than the observed W2, causing the separation between the simulated and observed paths to increase over time. Hence, varying the PBL scheme also changed the way the model handled W2, with the MRF simulation once again producing the best overall evolution of this wave.

A third shortwave, hereafter referred to as W3, developed to the south of the W1/W2 couplet and gradually propagated to the northeast as it deepened and became a closed low, reaching its maximum strength between 1200 UTC and 1800 UTC on 10 January. The path and central pressure tendency of W3

are shown in Figs. 1, 2, and 9d and 10d, respectively. All four simulations also developed a closed low feature corresponding to the observed W3, but the simulated W3s all traced a path further to the west than that observed, with the GYS and BKT W3s being the farthest to the west and the MRF W3 generally being the farthest to the east (best agreement with the observed path). Note that in addition to its path being displaced farther to the west, the location of the BKT W3, and to a smaller degree the GYS W3, lead that of the observed W3. And finally, it is important to note that although the propagation characteristics of the BLK W3 were only slightly worse than that of the MRF W3, the BLK simulation generates other short-wave features associated with the development of W3 that do not appear in the analysis fields. Although varying the PBL scheme did produce some minor differences in the way the model handled W3, the tendency for the behavior of W3 to be more consistent between the various simulations than was found for W1 and W2 suggests that the PBL schemes did not play a major role in determining how the model handles the evolution of this wave.

4.4 *Simulated Surface and PBL Structure*

Since the MRF simulation produced the best wave development and track, this simulation is used to illustrate the simulated structures and processes.

The three frontal waves produced by simulation MRF are discernible at the *R/V Knorr* location. However, the transitions at the surface were not nearly as sharp or obvious as in the observations and occur at different times (compare Figs. 4 and 11). For instance, the simulated surface pressure trace didn't show each individual trough as clearly, and the temperature and moisture transitions with each trough were smaller in the simulations.

The three waves show up more clearly in the time-height cross-sections at the *Knorr* location, especially in the temperature and wind fields (Fig. 12). However, there are also significant differences with the observations. The prefrontal warming associated with wave W2 is much weaker in the simulation (compare Figs. 5 and 12) and is mainly seen only below 1000 m, and the warming ahead of wave W1 is greater than observed. Secondly, the near-surface moisture plume associated with wave W2 is absent, as is the one for wave W3. Thirdly, wave W1 has no LLJ maximum and the low-level wind speed is significantly greater than in the observations.

All the simulations produce cloud base heights that are generally lower than those observed. The MRF simulation produces those that are in best agreement of the four simulations. For instance, in the prefrontal environment of wave W1, the MRF simulation produces cloud bases of 600-1200 m, in good agreement with those observed. However, the postfrontal environments in simulation MRF have cloud bases between 500-1300 m, substantially lower than those observed. Of the other simulations, only GYS produced post-frontal cloud base heights between 1000-2000 m, in better
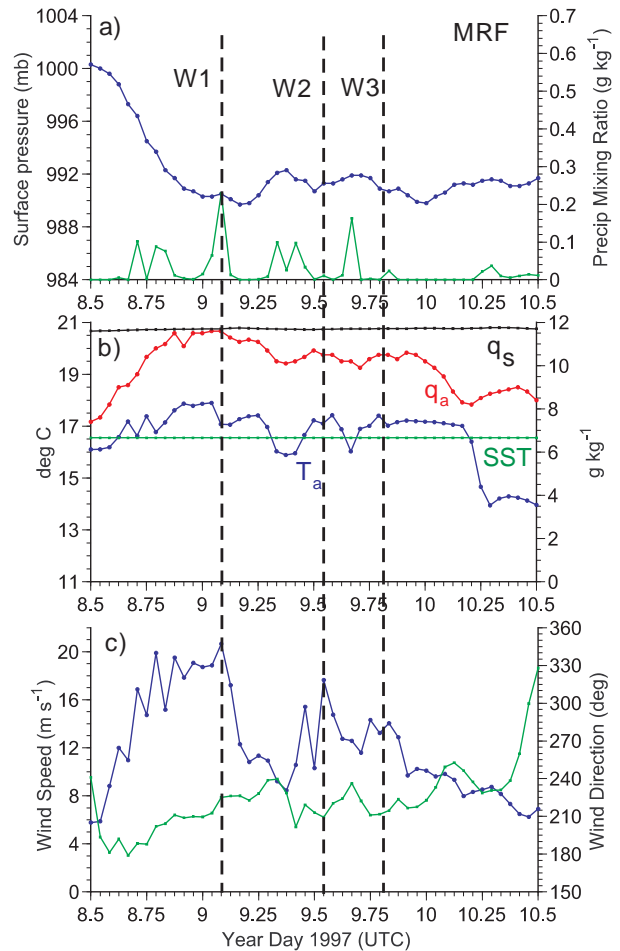

Fig. 11: The surface environment in simulation MRF at the location of the Knorr. *Shown are a) surface pressure (blue) and precipitation mixing ratio (green), b) 10-m air temperature (Ta), sea-surface temperature (SST), 10-m air specific humidity (qa), and surface specific humidity (qs), and c) 10-m wind speed (blue) and wind direction (green). The approximate time of passage of fronts associated with each frontal wave W1-W3 at the surface are indicated by the vertical dashed lines.*

agreement with the observations. The GYS prefrontal cloud bases were lower than those for MRF, however.

4.5 *Surface Fluxes with the Different PBL Schemes*

The differences between the four MM5 simulations can be due to either differences in the surface flux schemes associated with each PBL scheme, in the PBL scheme itself and how each of them redistribute the momentum, sensible heat and moisture in the vertical, or in both. To isolate the effect of the surface fluxes, offline versions of the Blackadar surface flux scheme (Grell, et al 1994) and the COARE3.0 flux scheme (Fairall et al, 2003) were used. First, the model output bulk parameters (e.g., air temperature, SST, wind speed, mixing ratio) from simulation MRF at the location of the *Knorr* were
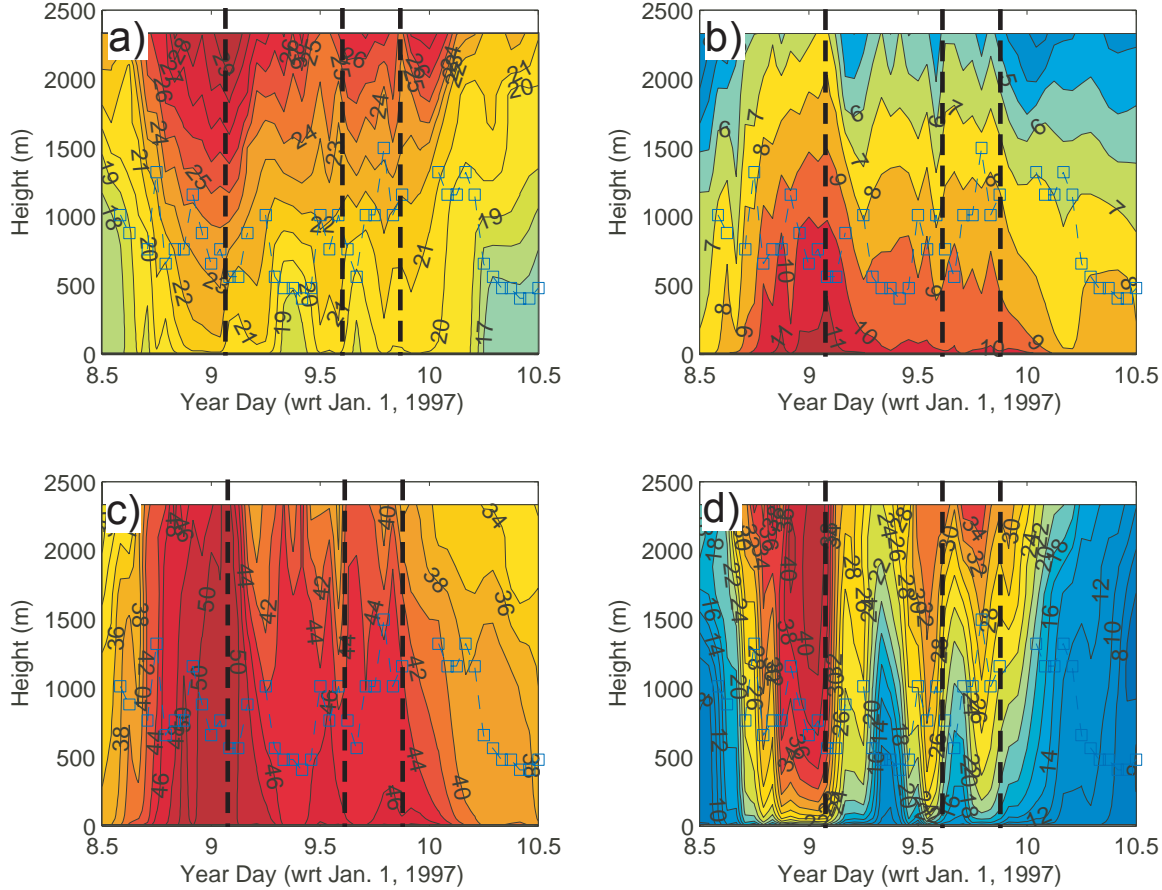
Fig. 12: As for Fig. 5, but for simulation MRF. The cloud base height (blue squares) was determined as the lowest height for which the cloud water mixing ratio was > 0.01 g kg^{-1}.

used as input parameters to the offline schemes to verify that the fluxes from the Blackadar offline flux scheme were in agreement with those from the MRF PBL scheme (which uses the Blackadar surface flux scheme). This test also showed that the COARE3.0 fluxes were substantially different. Then, to test which surface flux scheme performs better in this case, each of the offline schemes were used with the observed bulk parameters as input, and the observed covariance and inertial dissipation fluxes were used for validation.

Significant differences were again noted between the two schemes, especially for H_s and H_l (Fig. 7). Bin-averaged comparisons between the observations and the two bulk flux algorithms (Fig. 13) show that replacing the BLK surface flux scheme in the MRF, BLK, and GYS PBL schemes should provide more accurate surface fluxes, especially for H_l, and can potentially improve the simulations. Such an effort is underway and will be reported on during the presentation. Though the data base for the differences shown in Fig. 13 is limited, similar plots are obtained if the comparison includes the entire FASTEX time period from the *Knorr*.

5. CONCLUSIONS

FASTEX IOP1 consisted of a large cyclone in central North Atlantic with three frontal waves. Tracks of all of the waves were just on the warm side of the large SST gradient between the cold Labrador current and the relatively warm Atlantic Gulfstream. Wave W1 showed the greatest deepening, and downstream MSA measurements of IOP1 were focused on wave W2. However, the entire sequence of waves and their respective developments are important. Near surface data at 19 m height from the *R/V Knorr* showed distinct pressure troughs with each wave, 3-5 °C air temperature and 2-3 g kg^{-1} mixing ratio drops with each front, and distinct wind speed peaks of 17-19 m s^{-1} in the warm sectors associated with waves W1 and W2. Wave W3 passed directly over the *Knorr*. The soundings reveal the more occluded nature of the air passing over the *Knorr* with wave W3 in comparison to that associated with waves W1 and W2. Boundary layer depths and cloud bases were typically 700-1200 m in the prefrontal regions of each wave and 800-2000 m in the post-frontal regions. Surface fluxes were strongly
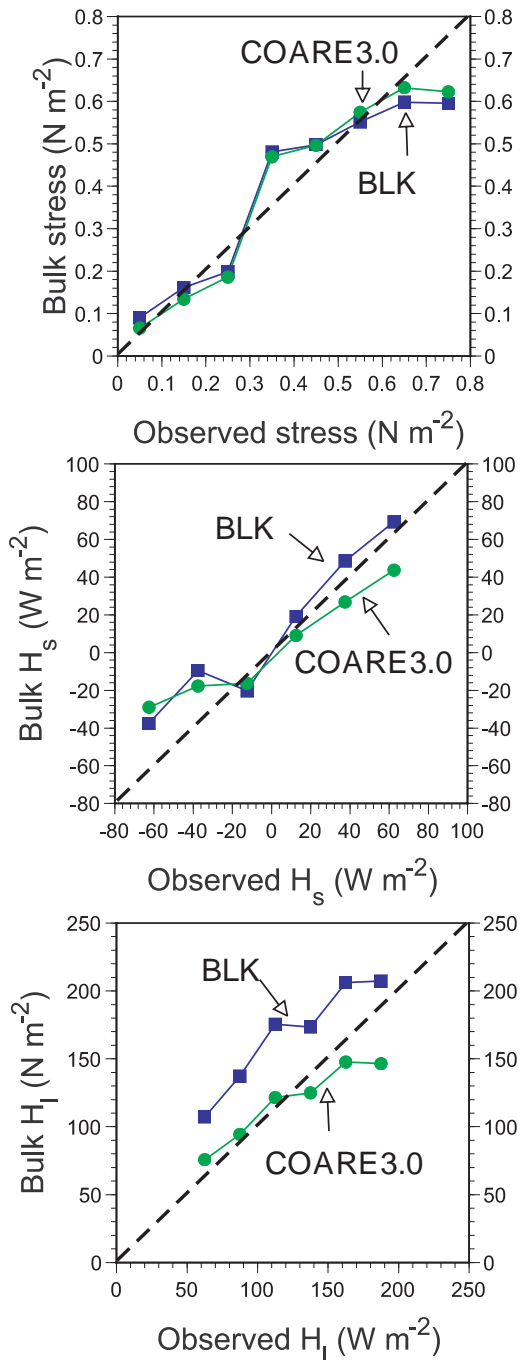
Fig. 13: Bin-averaged bulk fluxes as a function of the observed covariance and inertial dissipation fluxes from the R/V Knorr *from 12 UTC Jan. 8 - 12 UTC Jan. 10, 1997. Only flux bins containing at least 2 hourly points were used in the bin averaging.*

modulated by the synoptic and surface environment, with warm sector regions showing large surface stresses of 0.6-1.2 N m^{-2}, sensible heat fluxes of -50 - +10 W m^{-2}, and latent heat fluxes of 50-150 W m^{-2}. In the post-frontal regions, the stresses were substantially

less but the sensible and latent heat fluxes increased by 50-150 W m^{-2}.

MM5 simulations of this case were able to replicate the presence of the frontal waves, but using different PBL schemes produced different evolutions. None of the simulations were able to produce the correct track and central pressure for all three waves. Of the four PBL schemes considered in this study, the evolution of W1-W3 in the MRF simulation was, for the most part, the best match to the observed behavior of the three waves. Varying the PBL scheme had the largest impact on the evolution of waves W1 and W2. The track of W1 in the MRF simulation stands out as the clear winner, whereas the MRF and BLK simulations handled the track of W2 in a similar manner, but subtle timing issues once again point to the MRF simulation as the best match for the observed evolution. And finally, it is interesting to note that at least with respect to the paths of W1 and W2, the BKT and GYS simulations exhibited very similar erroneous tendencies, possibly pointing to a problem common to these two PBL schemes.

Comparisons of the simulated surface environment and vertical structures after 24-72 hours of simulation to the point measurements at the *R/V Knorr* were not impressive. This is partially due to the ample time for the initial condition errors and various process errors to produce large timing and spatial errors at the location of the *Knorr*. Near-surface variations associated with the frontal waves appeared damped in the simulations compared to the observations. Cloud bases and PBL heights tended to be lower than in the observations. Simulation MRF reproduced the PBL and cloud heights best.

Bulk surface fluxes in simulations MRF, BLK, and GYS are all computed by the Blackadar surface flux scheme. Using the covariance and inertial dissipation fluxes measured by the instruments on the Knorr, it has been shown that the Blackadar fluxes, especially for latent heat, have a significant error. Improved surface fluxes should be obtained by using an alternative surface flux scheme such as the COARE3.0 scheme (Fairall et al 2003).

However, it is uncertain how much improvement in the simulations will be produced by improving the surface fluxes. Additional differences between PBL schemes in the parameterization of the vertical transport of heat, momentum, and moisture within the boundary layer have significant impacts on the development and tracks of these frontal waves. This is clearly shown by the significant differences between simulations MRF and GYS, including the erroneous strong development of wave W2 in simulation GYS. Both simulations MRF and GYS use the Blackadar surface flux scheme. Results from tests incorporating the COARE3.0 surface flux scheme into the MM5 PBL schemes are currently being done, and the results will be presented at the conference.

6. REFERENCES

Benjamin, S. G., and N. L. Seaman, 1985: A simple scheme for objective analysis in curved flow. *Mon. Wea. Rev.*, **113**, 1184-1198.

Blackadar, A. K., 1976: Modeling the nocturnal boundary layer. *Proceedings of the Third Symposium on Atmospheric Turbulence, Diffusion and Air Quality*, pp. 46-49, Amer. Meteor. Soc., Boston, Mass.

Burk, S. D, and W. T. Thompson, 1989: A vertically nested regional numerical prediction model with second-order closure physics. *Mon. Wea. Rev.*, **117**, 2305-2324.

Fairall, C. W., E. F. Bradley, J. E. Hare, A. A. Grachev, and J. B. Edson, 2003: Bulk parameterization of air-sea fluxes: Updates and verification for the COARE algorithm. *J. Clim.*, in press

Grell, G. A., 1993: Prognostic evaluation of assumptions used by cumulus parameterizations. *Mon. Wea. Rev.*, **121**, 764-787.

_____, J. Dudhia, and D. R. Stauffer, 1994: A description of the fifth-generation Penn State/NCAR Mesoscale Model (MM5). *NCAR Technical Note*, NCAR/TN-398+STR. [Available from NCAR Publication Office, Box 3000, Boulder, CO 80303]

Hare, J. E., P. O. G. Persson, C. W. Fairall, amd J. B. Edson, 1999: Behavior of Charnock's relationship for high wind conditions. *Preprints, 13th Symp. on Bound. Layers and Turbulence*, Jan. 10-15, 1999, Dallas, TX, 252-255.

Hong, S.-Y., and H.-L. Pan, 1996: Nonlocal boundary layer vertical diffusion in a medium-range forecast model. *Mon. Wea. Rev.*, **124**, 2322-2339.

Joly, A., K. A. Browning, P. Bessemoulin, J.-P. Cammas, G. Caniaux, J.-P. Chalon, S. A. Clough, R. Dirks, K. A. Emanuel, L. Eymard, R. Gall, T. Hewson, P. H. Hildebrand, D. Jorgensen, F. Lalaurette, R. H. Langland, Y. Lemaître, P. Mascart, J. A. Moore, P. O. G. Persson, F. Roux, M. A. Shapiro, C. Snyder, Z. Toth, and R. Wakimoto, 1999: Overview of the field phase of the Fronts and Atlantic Storm-Track Experiment (FASTEX) project. *Quart. J. Roy. Meteor. Soc.*, **125**, 3131-3163.

Klemp, J. B., and D. R. Durran, 1983: An upper boundary condition permitting internal gravity wave radiation in numerical mesoscale models. *Mon. Wea. Rev.*, **111**, 430-444.

Kuo, Y.-H., R. J. Reed, and S. Low-Nam, 1991: Effects of surface energy fluxes during the early development and rapid intensification stages of seven explosive cyclones in the western Atlantic. *Mon. Wea. Rev.*, **119**, 457-476.

Louis, J. F., 1979: A parametric model of vertical eddy fluxes in the atmosphere. *Bound.-Layer Meteor.*, **17**, 187-202.

Persson, P. O. G., J. E. Hare, C. W. Fairall, S. Ataturk, and K. Katsaros, 1997: Air-sea interaction measurements during the Fronts and Atlantic Storm Tracks Experiment (FASTEX). *Preprints, 12th Symposium on Boundary Layers and Turbulence*, Vancouver, Canada, 28 July-1-Aug., 1997, 415-416.

_____, _____, _____, and W. Otto, 2003a: Air-sea interaction processes in warm and cold sectors of extratropical cyclonic storms observed during FASTEX. *Preprints, 12th Conference on Interactions of the Sea and Atmosphere*, AMS Annual Meeting, 9-13 Feb. 2003, Long Beach, CA.

_____, _____, _____, and _____, 2003b: Air-sea interaction processes in warm and cold sectors of extratropical cyclonic storms observed during FASTEX. *Quart. J. Roy. Meteor. Soc.*, In preparation.

Reisner, J., R. M. Rasmussen, and R. T. Bruintjes, 1998: Explicit forecasting of supercooled liquid water in winter storms using the MM5 mesoscale model. *Q. J. R. Meteorol. Soc.*, **124(548 Part B)**, 1071-1107.

Shafran, P.C., N.L. Seaman, and G.A. Gayno, 2000: Evaluation of numerical predictions of boundary-layer structure during the Lake Michigan Ozone Study (LMOS). *J. Appl. Meteorol.*, **39**, 412-426.

Zhang, D.-L., and R. A. Anthes, 1982: A high-resolution model of the planetary boundary layer-sensitivity tests and comparisons with SESAME-79 data. *J. Appl. Meteor.*, **21**, 1594-1609

Acknowledgements